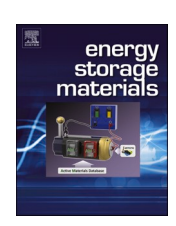
\$ SUPER

Contents lists available at ScienceDirect

Energy Storage Materials

journal homepage: www.elsevier.com/locate/ensm



The impact of lithium carbonate on tape cast LLZO battery separators: A balanced interplay between lithium loss and relithiation

Kaouther Touidjine ^{a,b,c,1}, Melanie Finsterbusch-Rosen ^{a,1}, Vivien Kiyek ^a, Swapna Ganapathy ^b, Martin Finsterbusch ^{a,d}, Olivier Guillon ^{a,d}, Mark Huijben ^c, Erik Kelder ^b, Marnix Wagemaker ^b, Dina Fattakhova-Rohlfing ^{a,d,e,*}

- ^a Forschungszentrum Jülich GmbH, Institute of Energy and Climate Research: Materials Synthesis and Processing (IEK-1), Wilhelm-Johnen-Straße, Jülich 52428, Germany
- b Delft University of Technology, Faculty of Applied Science, Department of Radiation Science and Technology, Delft, the Netherlands
- ^c MESA+ Institute for Nanotechnology, University of Twente, P. O. Box 217, Enschede 7500AE, the Netherlands
- d Helmholtz Institute Münster: Ionics in Energy Storage (IEK-12), Forschungszentrum Jülich GmbH, Corrensstr. 46, Münster 48149, Germany
- e University Duisburg-Essen, Faculty of Engineering and Center for Nanointegration Duisburg-Essen CENIDE, Lotharstraße 1, Duisburg 47057, Germany

ARTICLE INFO

Key words: LLZO Solid-state batteries Tape-casting Lithium loss Protonation, Sintering

ABSTRACT

Ceramic membranes made of garnet $\text{Li}_7\text{Zr}_3\text{La}_2\text{O}_{12}$ (LLZO) are promising separators for lithium metal batteries because they are chemically stable to lithium metal and can resist the growth of lithium dendrites. Free-standing garnet separators can be produced on a large scale using tape casting and sintering slurries containing LLZO powder, but the quality of the separators is severely compromized by the protonation of the moisture-sensitive LLZO during processing and the irreversible loss of lithium during sintering. In this work, an approach is presented to mitigate the degradation of the LLZO and produce high quality separators using Li_2CO_3 as a source of excess lithium. By systematically investigating the effects of Li_2CO_3 addition during the different steps of the tape casting process and the intricate relationship between the protonation and relithiation of LLZO phase, the formation of highly protonated LLZO during ball milling was identified as the most critical step. It was shown that the addition of minimal amounts of Li_2CO_3 during wet milling effectively suppresses LLZO protonation and ensure the effectiveness of relithiation during subsequent sintering. Using this modified method, flat LLZO separators with a relative density of 95.3 % were prepared in a simplified process with a significantly reduced excess lithium of only 5 mol % with respect to the stoichiometric LLZO, exhibiting an ionic conductivity of 0.18 mS cm⁻¹ at room temperature and a critical current density of 1 mA cm⁻² at 60 °C for lithium stripping/plating.

1. Introduction

Driven by the demands of the rapidly growing market for battery-powered devices, increasing the energy density of batteries is one of the most important development goals. Using lithium metal anodes instead of graphite is widely recognized as an efficient means of achieving this aim. Attempts to use lithium anodes in conventional lithium-ion battery designs have not yet been successful due to fundamental problems with lithium metal [1] In particular, the uneven stripping and plating of Lithium during multiple charges and discharges leads to the growth of so-called mossy or dendritic Lithium, which punctures the battery's soft polymer separators, causing short circuits

and endangering the battery [2] Therefore, ceramic separators that can resist dendrite growth and mechanically protect the cell are one of the most intensively pursued directions in developing lithium-metal batteries.

The typical material for ceramic separators is garnet $\rm Li_7Zr_3La_2O_{12}$ (LLZO), which has sufficiently high ionic conductivity and remarkably high chemical stability to Li-metal (6 V vs. Li) [3] . Numerous publications show that LLZO separators can be operated in symmetrical cells with Li electrodes for several hundred cycles and achieve critical current densities (CCDs) up to 100 mA cm $^{-2}$ [4]. For industrial applications, fabrication techniques enabling large-scale LLZO separator production is another important research goal. Among several possibilities,

 $\textit{E-mail address:} \ d. fattakhova@fz-juelich.de \ (D.\ Fattakhova-Rohlfing).$

 $^{^{\}star}$ Corresponding author.

¹ These authors contributed equally to the work.

tape-casting stands out as a well-known technique for the large-scale production of free-standing ceramic membranes, including LLZO separators [5–8]. In this process, large-area ceramic sheets are cast in a continuous process from a slurry containing ceramic powder, dispersant, binder, and plasticizer in a suitable solvent. To obtain pure ceramic components, the so-called "green tapes" must be sintered at high temperatures to remove organic components and compact the ceramic powder, resulting in dense, mechanically stable, free-standing separators.

The technical challenges in producing high-quality LLZO separators are related to the high mobility of the lithium ions and the high temperatures of up to 1200 °C [5,6,8] required for sintering LLZO. LLZO is chemically stable at ambient conditions but is readily protonated upon contact with water [6] (including moisture [7–11]), carbon dixode [12], and protic solvents [13] resulting in lithium leakage from the structure due to Li⁺/H⁺ exchange. Although protonated LLZO can be reversibly relithiated. Unwanted decomposition can occur if the lithium-ion concentration is insufficient for this reaction (which is often the case at high temperatures due to the volatility of Li compounds) [13] The cumulative effect of unwanted Li loss from the LLZO structure during the various fabrication steps results in suboptimal sintering activity, negatively affecting the relative density, flatness, ionic conductivity [14,15], mechanical stability, and electrochemical performance of LLZO separators [16,17]. It should be noted that although Li loss is a common problem in the fabrication of LLZO-based components, it becomes even more critical in the fabrication of thin LLZO separators due to their high surface-to-volume ratio.

To compensate for the loss of Li, an excess Li concentration is usually required when synthesizing LLZO powders and processing them into ceramic components. Depending on the synthesis method and processing conditions, the excess Lithium can vary between 10 wt % [14,16,18] and up to 50 wt % [15], which increases the synthesis and manufacturing cost. In addition to the higher costs, the chemical composition and concentration of the compounds used as a lithium source affect the separator properties by changing the composition of the grain boundaries, introducing additional phases, and sometimes leading to additional porosity [19]. Table 1 gives an overview of the state of the art for tape-casting of LLZO separators, correlating the used lithium-excess and the resulting electrochemical properties. No obvious ideal lithium-excess can be determined form literature analysis, strongly indicating the need for a detailed analysis of the whole process chain, combined with an optimization of the tape-casting procedure to obtain dense, flat separators with good electrochemical performance in a simplified process with reduced excess Li is therefore important to improve their performance and to increase the economic competitiveness of LLZO separators.

In this work, we present an approach to prepare LLZO separators in a simplified tape-casting process with a reduced Li excess using lithium carbonate as an additional Li source, which was selected based on its

Table 1Examples of lithium excess used in fabrication of thin LLZO separators.

Composition	Li excess [mol %]	Ionic conductivity [mS cm ⁻¹]	CCD [mA cm ⁻²]	Reference
Li _{6.25} Al _{0.25} La ₃ Zr ₂ O ₁₂	50	0.2	n.d.	[15]
Li _{6.5} Al _{0.25} La ₃ Zr ₂ O ₁₂	10, 15, 20	0.3	n.d.	[14]
$\text{Li}_{6.4}\text{La}_{3}\text{Zr}_{1.4}\text{Ta}_{0.6}\text{O}_{12}$	16	0.5	0.05 at 60 °C	[19]
$Li_{6.45}Al_{0.05}La_{3}Zr_{1.6}Ta_{0.4}O_{12}$	20	0.15	0.02 at 60 °C	[20]
$\text{Li}_{6.45}\text{Al}_{0.05}\text{La}_{3}\text{Zr}_{1.6}\text{Ta}_{0.4}\text{O}_{12}$	20	0.39	0.3 at 60 °C	[21]
Li _{6.75} La _{2.75} Ca _{0.25} Zr _{1.5} Nb _{0.5} O ₁₂	10	n.d.	10 in 3D network	[22]

chemical similarity to the native compound formed on the LLZO surface and its neutral pH value. By systematically studying the effect of $\rm Li_2CO_3$ introduced in the different steps of the tape-casting process and evaluating the LLZO composition after each step, we were able to reduce the effective amount of additional $\rm Li_2CO_3$ to only 1,3 wt % in the processing mixture, corresponding to a total Li excess of 15 mol % and optimize the processing conditions to obtain flat and dense LLZO separators capable of reaching 1 mA cm $^{-2}$ in symmetrical cells with Li electrodes.

2. Experimental part

Powder synthesis. Li_{6.45}Al_{0.05}La₃Zr_{1.6}Ta_{0.4}O₁₂ starting powder was prepared via solid-state synthesis. Stoichiometric amounts of LiOH•H₂O (Applichem, 99 %), La₂O₃ (Merck, 99 %, pre-dried at 900 °C for 10 h), ZrO₂ (Treibacher, 99,7 %), Ta₂O₅ (Treibacher, 99,95 %) and Al₂O₃ (Inframat, 99,82 %) were used. 10 wt % excess of LiOH was added to compensate for lithium evaporation during high-temperature treatment. The mixture was thoroughly mixed (Retsch, 200 M) and pressed into pellets before the first calcination step at 850 °C for 20 h. The obtained pellets were crushed (Retsch, BB50) and dry-milled (Retsch, PM400) in 250 ml tungsten carbide jars with 20 mm tungsten carbide milling balls at 200 rpm and subsequently sieved with a 50 μ m mesh (Fritsch, Analysette). The obtained powder was pressed into pellets and calcined a second time at 1000 °C for 20 h. Afterward, the pellets were crushed and dry-milled again.

To reduce the particle size of the powder dedicated to the tape-casting process, some of the starting powder was dry-milled (Fritsch, Pulverisette 7) at 500 rpm for 230 min in a 80 ml $\rm ZrO_2$ milling jar with 3 mm milling balls. Another part of the starting powder was wet-milled in ethanol with the same set of parameters. The wet-milled powder was subsequently dried in air at 70 °C for at least 12 h. The dried powder was annealed in an $\rm Al_2O_3$ crucible in air at 750 °C for 2 h with heating and cooling rates of 5 K min $^{-1}$.

2.1. Sample preparation

LLZO pellet preparation: The powder used for pellets preparation was used without milling. The starting powder was uniaxially pressed into pellets of 13 mm diameter at 120 MPa. The pellets were placed on a MgO plate with a bed of the starting powder in a closed Al_2O_3 crucible and sintered at 1175 $^{\circ}\text{C}$ for 10 h with heating and cooling rates of 5 K min $^{-1}$.

Thin separator preparation: For the tape-casting process, a solution of the dispersant (BYK 180, Altana), binder (PVB98, Sigma Aldrich), and additives (PEG400, Sigma-Aldrich and Solusolv, Solutia Inc.) in a mixture of ethanol (VWR, 99,6 %) and butanone (VWR, 99,6 %) in weight % ratios of (7.9:12.7:79) was prepared beforehand and mixed on a roller bench for at least 24 h. The same batch of polymer solution was used for all samples.

To prepare the slurries, the wet-milled or dry-milled LLZO powder was added to the solution and homogenized in a planetary mixer (Thinky) at 1500 rpm for 2 min. The same batch of polymer solution was used for all samples, and the ratio of LLZO powder to binder solution (1:0.6) was kept constant. The obtained slurry was cast onto a mylar foil. The gap height was fixed to 350 μm and kept constant for all samples. After drying for at least 4 h at room temperature, the obtained green tapes were compacted and laminated with 500 MPa at 80 °C for 2 min. After pressing, the green tapes were cut into 9 mm or 12 mm diameter discs, placed on a starting powder bed on a MgO plate in a closed Al_2O_3 crucible, and sintered in air at 1175 °C for 10 h with heating and cooling rates of 5 K min $^{-1}$.

Characterization. The particle size distribution of the starting powder and the two milled powders was checked via laser diffraction using a LA950 (Horiba Scientific) with a 650 nm and a 405 nm laser source, and data were analyzed via Mie-theory. Phase purity was determined by X-ray diffraction (XRD) analysis with a Bruker D4 Endeavor (Supp 2)

equipped with a 1D detector LYNXEY using monochromatized Cu K α radiation. Chromatic white light interferometry (CT-350, cyber scan with CHR-1000 sensor) was used to characterize the surface topography.

To obtain information on the protonation of the powder surface, Raman spectra were collected using a Renishaw INVIA Raman Microscope equipped with a solid-state excitation laser (532 nm) and a 2400 lines/mm grating. The measurement was conducted at a laser power of 2.5 mW to avoid laser-induced damage of the material. The exposure time was 1 s per spectrum. The cosmic rays of the raw data were removed using the Wire 5.2 software function (Renishaw). The spectra were normalized to the maximum height between $600\ cm^{-1}$ and $700\$ cm⁻¹. To analyze the microstructure of the separators, the samples were embedded in epoxy resin (EpoFix) and mirror-polished for microstructure analysis. The microstructure was analyzed via scanning electron microscopy (Carl Zeiss Microscopy, Zeiss EVO 15) and an energydispersive X-ray spectroscopy detector X-max 80 (Oxford Instruments plc, Abingdon, UK). The sample density was determined by analyzing cross-section images through the ImageJ software. The topography of the sintered samples was analyzed using an optical profilometer with a P-CHR-10,000 sensor (Model CT350T, cyberTECHNOLOGIES GmbH,

For electrochemical characterization, the sintered pellets from the starting powder were dry-polished up to 4000 grit. The sintered tapes were too thin for mechanical surface treatment and were used as received. Blocking electrodes were applied by sputtering gold onto the fresh surface (2 min sputter time, Cressington 108auto Coater). Using a BioLogic VMP-300 multi-potentiostat, the room temperature impedance of the pellets was measured. The frequency was varied from 7 MHz to 1 Hz with an electrical field perturbation of 10 mV mm $^{-1}$. All graphs were normalized to the sample's thickness. All measurements were fitted using the Relaxis software to extract resistance and conductivity. Each semi-circle was fitted using a CPE element, where the real capacitance was calculated as $C = \frac{(QR)^{1/a}}{R}$, with the resistance R, the pseudocapacitance Q, and the exponential parameter α derived from the data fit. The ionic conductivities were calculated using the formula $\sigma = \frac{dR}{A}$, where R is the resistance, d is the sample thickness, and A is the sample area.

To investigate dendrite formation, symmetrical Li|LLZO|Li cells were assembled under an argon atmosphere. A thin gold interlayer was sputtered onto the sample surface (~30 nm, Cressington 108auto Coater). Freshly calendared metallic Lithium was pressed on each side by hand. The sample was then placed between two Ni discs, and the stack was heated to 300 °C and subsequently cooled to 180 °C, 75 °C and 40 °C with 20 min of holding time each to ensure good mechanical and electrical contact. Critical current density measurements were conducted at 60 °C using the same multi-potentiostat mentioned above. Starting at $50\mu A~cm^{-2}$ for 1 h of plating and stripping time, the capacity of Lithium moved through the sample was kept constant by increasing the current by $50\mu A~cm^{-2}$ for each cycle and reducing the cycle time accordingly. All electrochemical measurements were carried out in a Swagelok cell.

Magic angle spinning (MAS) solid-state NMR measurements were performed on a Bruker Ascend 500 magnet ($B_0=11.7~T$) with a NEO console operating at frequencies of 500.13 MHz for 1H and 194.37 MHz for 7Li . Chemical shifts of 1H were referenced with respect to an external reference of adamantane. For 7Li a 0.1 M LiCl solution was used as the chemical shift reference. The samples were packed into 3.2 mm zirconia rotors, and a Bruker three-channel MAS 3.2 mm DVT probe was employed. All measurements were performed at a 20 kHz spinning speed. 1H spectra were recorded using a pulse sequence with background suppression to eliminate probe background where a pulse length of 3 μ s was utilized. 7Li spectra were recorded with a one-pulse experiment with a pulse length of 4 μ s. The recycle delay was set each time to three times T_1 , where T_1 was determined with a saturation recovery experiment.

3. Results and discussion

The starting powder in this study was synthesized with 10 % excess lithium to account for losses during the high-temperature treatments required to produce battery components from the solid electrolyte powder. This powder composition was found to be sufficient for the production of sintered LLZO components using dry processing routes such as dry powder pressing [10,23,24].

In solvent-based processes such as tape-casting, the excess usually needs to be higher as additional losses due to the ${\rm Li}^+/{\rm H}^+$ exchange in LLZO must be taken into account.

In contact with water or protic solvents, LiOH (Eq. (1a)) can be formed as intermediate products that react with CO_2 to form Li_2CO_3 (equations 1b) when exposed to ambient air [16,25,26].

$$\text{Li}_{7}\text{La}_{3}\text{Zr}_{2}\text{O}_{12} + x\text{H}_{2}\text{O} \rightarrow \text{Li}_{7-x}\text{H}_{x} \text{La}_{3}\text{Zr}_{2}\text{O}_{12} + x\text{LiOH}$$
 (1a)

$$LiOH + \frac{1}{2}CO_2 \rightarrow \frac{1}{2}H_2O + \frac{1}{2}Li_2CO_3$$
 (1b)

$$\text{Li}_{7\text{-x}} \, \text{H}_x \text{La}_3 \text{Zr}_2 \text{O}_{12} + \text{x}/2 \, \text{Li}_2 \text{CO}_3 \rightarrow \text{Li}_7 \text{La}_3 \text{Zr}_2 \text{O}_{12} + \text{x}/2 \, \text{H}_2 \text{O} + \text{x}/2 \, \text{CO}_2(2)$$

The protonation reactions are considered detrimental to the properties of LLZO and its further processing into battery components. However, these reactions can be reversed at a temperature above 400 °C [10,27] if a sufficient amount of Li source is added, restoring the structure and properties of the original LLZO (Eq. (2)). The reversibility of the relithiation process can generally be high in conventional processing, such as powder pressing and sintering, as the depth of the protonation reaction is limited to the surface, and only a minimal excess of Li is required to compensate for the volatility of Li₂CO₃. However, in solvent-based processing such as tape casting, the reaction proceeds mainly via the formation of soluble LiOH, which diffuses away from the surface, changing the local equilibrium and forcing more profound lithium depletion in the LLZO (Equation 1). If not enough Lithium is added during relithiation (e.g., due to increased volatilization of lithium compounds during sintering of thin porous tapes), the remaining protonated LLZO phase can decompose to La₂Zr₂O₇ [13,28]. In order to prevent such decomposition, a higher excess of Lithium is usually required in solvent-based processes [29,30].

To investigate the effects of the processing method on the properties of the separators produced from the LLZO powder described above, the differently treated powders were sintered at a temperature of 1175 °C for 10 h without an additional excess lithium source. The as-synthesized LLZO powder exhibits a particle size of about $D_{50}\!=\!8.6~\mu m$, which is too large for the fabrication of thin tapes. Therefore, part of the assynthesized powder was pressed into pellets as a reference sample, and the remaining parts were milled (dry and wet) to reduce the particle size, suitable for usage in the tape-casting process (Supplementary Figure 1).

The pellets produced from as-synthesized powders show good phase purity corresponding to cubic LLZO, with only minor secondary phases of LiAlO $_2$ due to Al uptake from the crucibles (Fig. 1) [16,31]. The cross-section of the pellet (Fig. 2a) shows high densification of the pellet with only 6 % remaining porosity. The Nyquist plots of the impedance spectra show only one semicircle containing contributions of bulk and grain boundary conductivity, which cannot be deconvoluted at room temperature. Therefore, a total ionic conductivity of 0.6 mS cm $^{-1}$ is derived from the low-frequency intercept.

In contrast to the as-synthesized powder, the tapes prepared from dry-milled and wet-milled powders exhibit lower phase purity. XRD analysis of the sintered tapes (Fig. 1a) shows the presence of $\rm Li_2CO_3$ and $\rm La_2Zr_2O_7$ in both samples, indicating a $\rm Li^+/H^+$ -exchange reaction and significant lithium loss during processing, as discussed above. The formation of protonated LLZO during milling and tape-casting is also reflected in lower sintering activity. The cross-section of both tapes (Fig. 2b,c) shows only minimal density with high residual porosity of 34 %. The Nyquist plots of the impedance spectra show two semicircles for

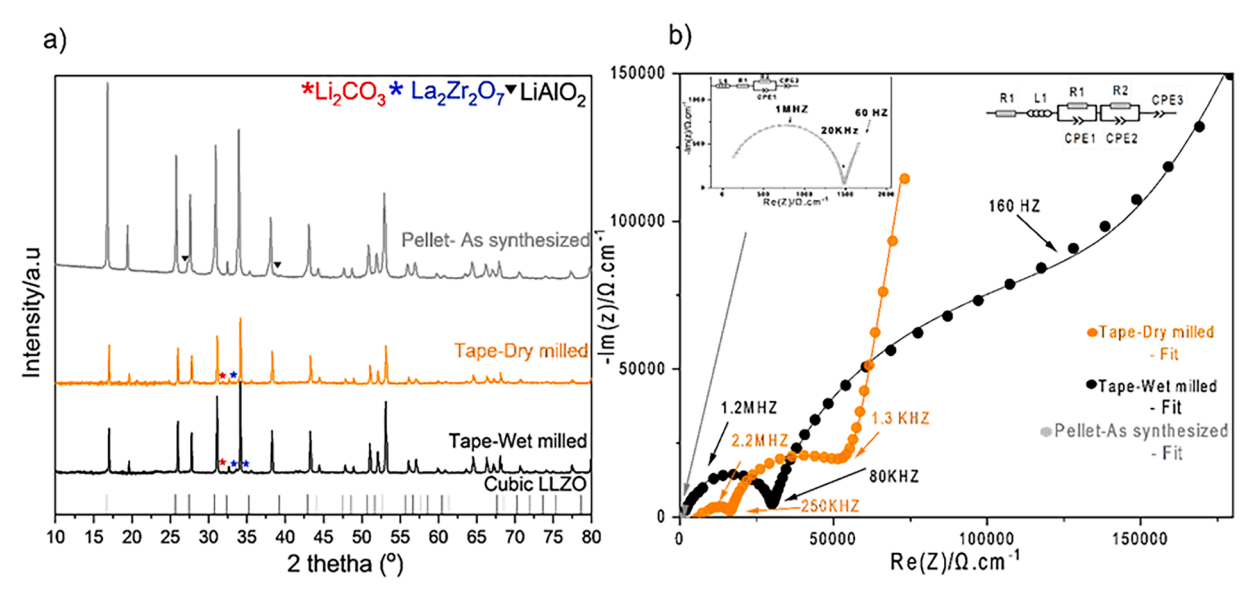


Fig. 1. a) XRD patterns and (b) Nyquist plots of the impedance spectra of the pressed pellet and tape cast LLZO separators from dry-milled and wet-milled powders.

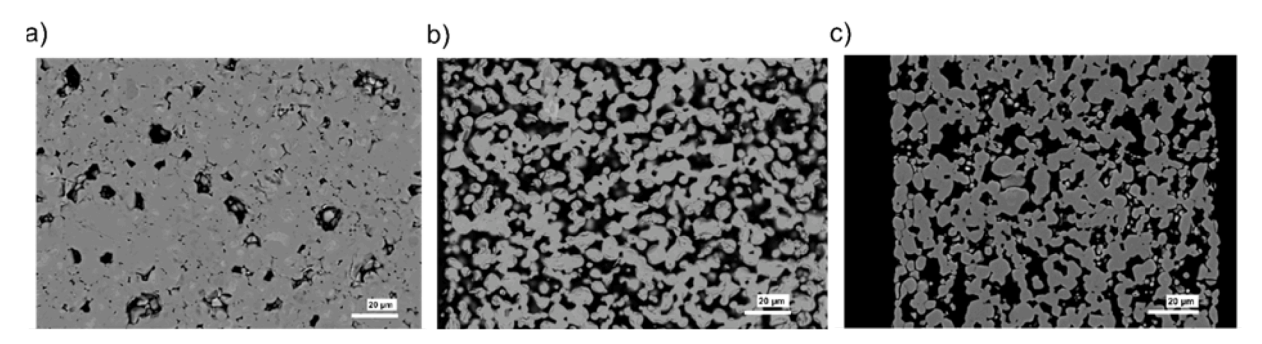


Fig. 2. Cross-sectional SEM images of the sintered LLZO separators prepared without any additional lithium excess. a) pressed pellet; b) tape from wet-milled powder; c) tape from dry-milled powder.

both samples, with the high-frequency semicircle corresponding to a bulk resistance (capacitance of 3.46 10^{-10} F for dry-milled and of 1.03 10^{-10} F for wet-milled) and the low frequency semicircle corresponding to grain boundary resistance (capacitance of 5.49 10^{-8} F for dry-milled

and of $4.15\ 10^{-8}$ F for wet-milled). The ionic conductivity calculated from the low-frequency intercept is $0.08\ mS\ cm^{-1}$ and $0.05\ mS\ cm^{-1}$ at room temperature for dry-milled and wet-milled samples, respectively, which is much lower than the ionic conductivity of the pellet made out

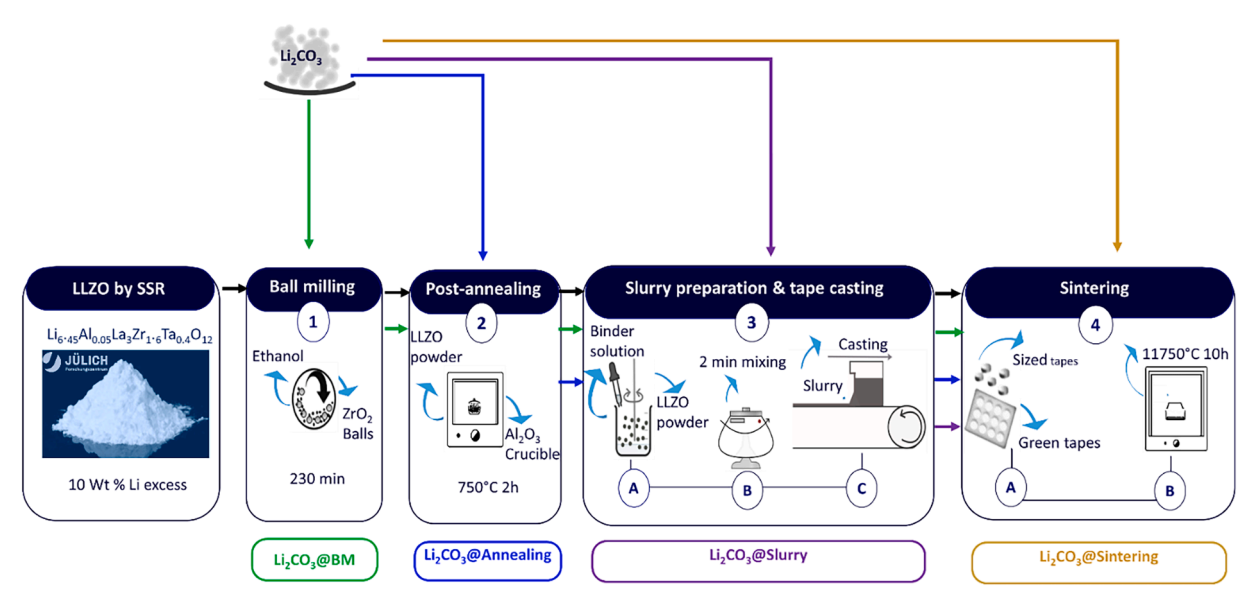


Fig. 3. Schematic overview of the main process steps in the studied tape-casting process and labeling of samples for different insertion points of Li₂CO₃.

of as-synthesized powder.

To reduce the loss of Lithium and minimize the resulting degradation of the electrochemical performance of tape-cast LLZO separators, an excess lithium source can be added to the LLZO powders during the various steps of the tape-casting process. The lithium compound used as a lithium source should not introduce impurities or additional phases into the LLZO structure, so the choice of anions in suitable lithium salts is limited to oxides, hydroxides, carbonates, or carboxylates, which can decompose to form volatile products. In this study, $\rm Li_2CO_3$ was chosen because it occurs naturally in the samples and Lithium can be easily integrated into the crystal structure during the relithiation of protonated LLZO. In addition, $\rm Li_2CO_3$ is neutral, does not change the pH of the tapecasting slurry like LiOH, and does not require additional optimization of the tape-casting process and the high-temperature treatment like LiCOOCH₃.

 ${\rm Li_2CO_3}$ can be introduced in various process steps, thereby possibly affecting the properties of the resulting separators. Four main process steps were identified as possible application points for the lithium source, namely ball milling, annealing, slurry preparation, and sintering (Fig. 3). Based on previous experiments [6,7], the amount of ${\rm Li_2CO_3}$ was set as 2.6 wt % with respect to the LLZO, which corresponds to an additional 10 mol % excess lithium with respect to the LLZO stoichiometry. The respective amount of ${\rm Li_2CO_3}$ was added during these critical

steps, and the properties of separators after sintering in the same conditions were analyzed to determine the impact on each point of the process. The tapes obtained in the processes in which Li₂CO₃ was added either during ball milling, annealing, slurry preparation, or sintering steps are assigned furtherasLi₂CO₃@BM, Li₂CO₃@annealing, Li₂CO₃@slurry, and Li₂CO₃@sintering, respectively.

XRD analysis of the sintered samples (Fig. 4a) shows that the phase composition of the sintered tapes resulting from all variants of the process route corresponds to cubic LLZO, indicating that Li2CO3 as an excess lithium source and the chosen concentration are suitable for the production of phase-pure LLZO separators. However, there are obvious differences in the morphology of the sintered tapes prepared via different modification routes (Fig. 6), confirming that the timing of the Li₂CO₃ addition is important for the final quality of separator. Adding Li₂CO₃ during the milling step leads to the highest density of the sintered tapes (Li₂CO₃@BM), as it significantly hinders the protonation of LLZO and the associated formation of La₂Zr₂O₇phase after ball milling (Fig. 4d). It can be assumed that adding Li₂CO₃ in this step shifts the equilibrium of the protonation reaction in ethanol towards LLZO, reducing the amount of protonated phase and thus minimizing the undesirable changes in the LLZO crystal structure. In contrast, the addition of Li₂CO₃ during the annealing step (Li₂CO₃@annealing) leads to the formation of LiAlO₂ as a secondary phase after annealing (Fig. 4c),

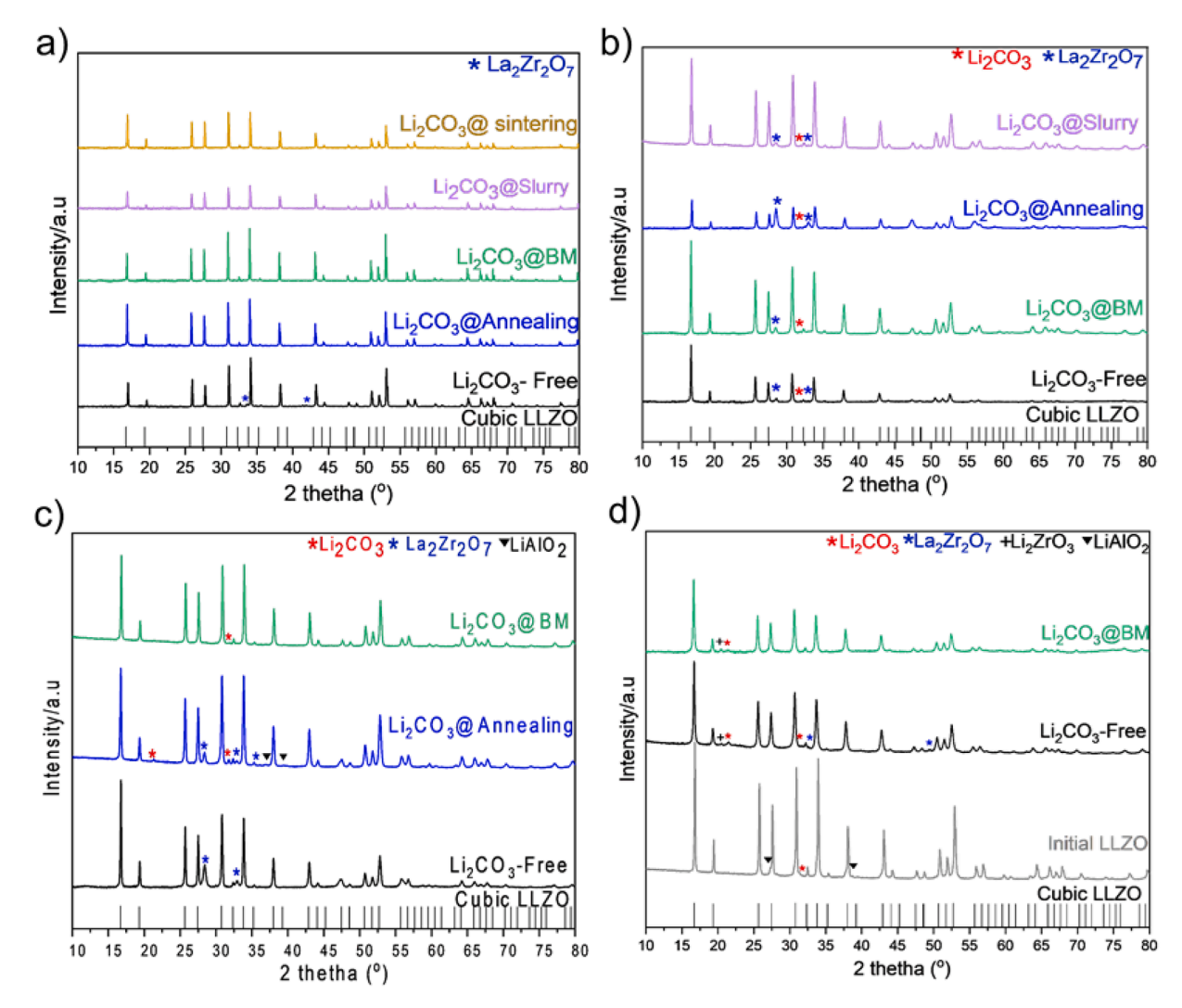


Fig. 4. XRD patterns of LLZO: a) sintered tapes; b) green tapes; c) powder after annealing; d) dried powder after ball-milling. Li_2CO_3 was added during ball milling $(Li_2CO_3@BM)$, green), annealing $(Li_2CO_3@annealing)$, blue), slurry preparation $(Li_2CO_3@slurry)$, purple) and sintering $(Li_2CO_3@sinter)$, yellow) as compared to the tape prepared in the same conditions but without addition of Li_2CO_3 (Li_2CO_3 -free). All tapes were sintered at 1175 °C for 10 h.

which may be due to the fact that the solid ${\rm Li_2CO_3}$ powder is less finely dispersed and can react with the alumina crucible. The process of ${\rm LiAlO_2}$ formation consumes lithium ions, which are therefore less available for the relithiation of the protonated LLZO and thus promote the formation of unfavorable secondary phases.

The XRD patterns of the green tapes display no significant changes compared to the annealed powders (Fig. 4d,c), as the dwell time of the LLZO material in the solvent is minimal during this step. Therefore, the spectra of ${\rm Li_2CO_3}$ @slurry are similar to ${\rm Li_2CO_3}$ -Free, as expected. Adding ${\rm Li_2CO_3}$ during sintering (${\rm Li_2CO_3}$ @sintering) is also effective in suppressing secondary phases in the sintered tape. It should be noted that the addition of excess Li in this step was realized by enriching the atmosphere with Lithium in the closed crucible, which promotes efficient relithiation of the tapes and suppresses the formation of secondary phases.

The XRD measurements show that addition of Li_2CO_3 in the ball milling step has the greatest effect on the proton exchange of LLZO and the formation of secondary phases, as it consistently has the least amount of detrimental reaction products. To further investigate the possible changes in the phase composition of LLZO during the Li_2CO_3 @BM process, LLZO powder was ball-milled in the presence of excess Li_2CO_3 and then dried and annealed at (750 °C, 2 h). The annealed powder was analyzed using Raman spectroscopy (Fig. 5a) and nuclear magnetic resonance (NMR) (Fig. 5b-c). Both techniques show the presence of LLZO as the dominant phase, indicating that this phase remains practically intact during all processing steps. In contrast, ball milling without Li_2CO_3 addition (powder_Li_2CO_3-free) leads to a strong protonation of the LLZO phase and the formation of $\text{La}_2\text{Zr}_2\text{O}_7$ after annealing, which is consistent with the results of the XRD analysis.

In addition, the characteristic peaks of Li₂CO₃ at 156 cm⁻¹, 194 cm⁻¹ and 1090 cm⁻¹ [32] in the Raman spectra indicate the presence of Li₂CO₃ on the surface of the particles. This is due to the handling of the powders, and since the Raman spectroscopy measurement is performed after annealing in ambient air, some Li⁺/H⁺ exchange is to be expected. Remarkably, a peak at 326 cm⁻¹, indicating the formation of a low-temperature cubic phase of LLZO (LT-LLZO) after the annealing of protonated LLZO [33-35] is present in both samples, but to a much lesser extent in the powder Li₂CO₃@BM sample. To confirm the correlation between the peak height and the delithiation depth in LLZO, the intensity of the Li⁺/H⁺-exchange reaction was artificially increased by adding 5 wt % of water to the milling process (H2O@BM). After annealing, the height of the peak at 326 cm⁻¹ increased significantly, confirming the correlation. In addition, a broad peak at 289 cm⁻¹, which is characteristic of the La₂Zr₂O₇ phase [36], can be seen in the powder processed without additional Li₂CO₃ (Li₂CO₋Fee), confirming the profound Li loss in this sample. It can be therefore safely concluded that the addition of ${\rm Li_2CO_3}$ during ball milling can significantly reduce the ${\rm Li^+/H^+}$ exchange during processing.

Solid-state ¹H NMR spectra of the powders that were ball-milled without the addition of Li₂CO₃ (powder Li₂CO₃-free) show a peak at 5.29 ppm attributed to protons in the LLZO lattice [37] with two shoulders at 3.65 ppm and 6.35 ppm, indicating the presence of protons at different sites in the LLZO lattice. Besides the main peak with high chemical shift, the spectra of Li₂CO₃-free as well as powder Li₂CO₃@BM samples show two narrow peaks at 1.2 ppm and 0.9 ppm, which are assigned to adsorbed water on the LLZO surface [38]. An additional peak at -2 ppm can be attributed to LiOH [37]. In contrast, the H—NMR peak shape of Li₂CO₃@BM sample demonstrates a narrower and singular component at 5.29 ppm, implying protons only occupying one site type in the LLZO lattice, suggesting that this sample has a higher Li amount (as confirmed by Li-NMR) compared to the untreated LLZO (Li₂CO₃--Free), where additional shoulders in the peak shape indicate other proton popularity occupying different sites. This indicates that the LLZO in this case, has numerous lithium site vacancies within the LLZO structure, prompting more protons to occupy the different sites at the expense of lithium leaching from the structure. Importantly, When Li₂CO₃ was added during ball milling (Li₂CO₃@BM), the intensity of the main peak at 5.29 ppm corresponding to the H-LLZO as well as the peaks corresponding to the absorbed protons decreased significantly, confirming the effective attenuation of Li⁺/H⁺ exchange during exposure to the solvent. ⁷Li-NMR spectrum of the powder_Li₂CO₃@BM sample shows a singular peak at 0.5 ppm corresponding to Li-ions in the LLZO lattice. In contrast, a very broad signal was observed in the ⁷Li-NMR spectrum of the powder_Li2CO3-free sample, possibly encompassing several distinct lithium environments. This suggests the formation of Li-containing impurity phases such as Li₂CO₃ or LiOH during heat treatment in the absence of a lithium-source or a re-distribution of Li in tetrahedral and octahedral LLZO sites, which occurs proton-exchanged LLZO [37]. The results of NMR spectroscopy confirm the results of the Raman spectroscopy and XRD measurements discussed

For use as separators in batteries, the sintered tapes must have low porosity and high flatness to withstand the mechanical stress during cell assembly, and they must be resistant to dendrite growth when combined with Li metal anodes. However, only the tapes prepared via the $\rm Li_2CO_3@BM$ route (where $\rm Li_2CO_3$ was added during wet ball milling) exhibit sufficient densification to serve as separators. The $\rm Li_2CO_3@BM$ samples have a relative porosity of 5.8 %, similar to the porosity achieved with conventionally pressed samples (Fig. 6a-e). The separators prepared by other routes show low relative densities with porosities above 35 %, although all samples were sintered under the same conditions and showed high phase purity in the XRD analysis. In addition, the

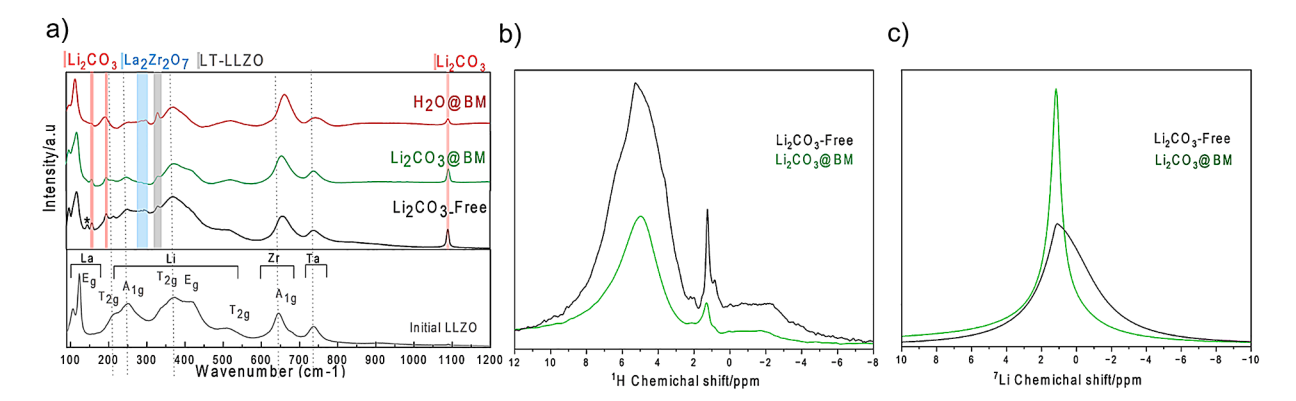


Fig. 5. a) Raman spectra of annealed LLZO powders wet-milled without the addition of $\text{Li}_{2}\text{CO}_{3}$ (powder_Li₂CO₃-free, black), with addition of Li₂CO₃ (powder_Li₂CO₃@BM, green), and without addition of Li₂CO₃ but with additional water (powder_H₂O@BM red); b) ¹H NMR spectra of annealed LLZO powders wet-milled without addition of Li₂CO₃ (powder_Li₂CO₃-free, black) and with addition of Li₂CO₃ (powder_Li₂CO₃@BM, green); c) ⁷Li-NMR spectra of annealed LLZO powders wet-milled without addition of Li₂CO₃ (powder_Li₂CO₃-free, black) and with addition of Li₂CO₃ (powder_Li₂CO₃@BM, green).

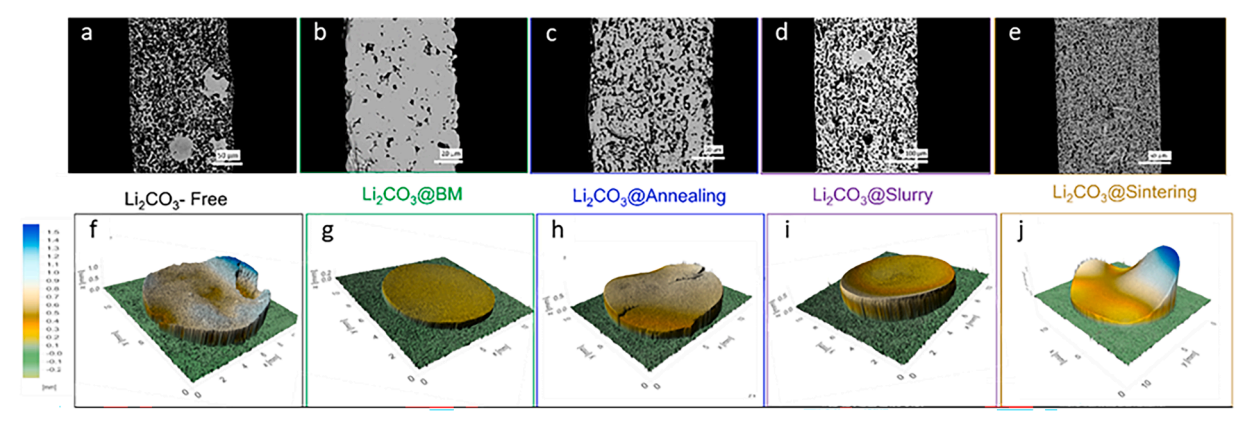


Fig. 6. Cross-sectional SEM images of sintered separators: a) wet-milled starting powder; b) Li₂CO₃@BM; c) Li₂CO₃@ Annealing; d) Li₂CO₃@ slurry; e) Li₂CO₃@ sintering. White light topography images of: f) wet-milled starting powder; g) Li₂CO₃@BM; h) Li₂CO₃@ Annealing; i) Li₂CO₃@ Slurry; j) Li₂CO₃@ Sintering.

porous samples show a strong warpage at the edges caused by inhomogeneous shrinkage, making cell assembly and electrochemical characterization impossible (Fig. 6f-j). This observation obviously indicates that the ${\rm Li}^+/{\rm H}^+$ -exchange and especially lithium loss are detrimental to the separator properties and should be limited throughout the process, as deep protonation and secondary phase formation, even if reversible, significantly hinder the sintering activity of LLZO.

By identifying the ball milling process as the pivotal step in the regulating of Li⁺/H⁺ exchange, there is a possibility to reduce the excess Lithium. In further experiments, the amount of Li₂CO₃ added during the ball-milling step was reduced by 50 %, corresponding to a lithium excess of only 5 mol % with respect to the stoichiometric LLZO. The XRD measurements after each processing step (Fig. 7a) consistently show a high phase purity over the entire process chain. Only the green tape shows minimal traces of La₂Zr₂O₇, which is consistent with the results for the original LLZO powder with a higher Li₂CO₃ content (Li₂CO₃@BM). SEM analysis of the cross-section shows a homogeneous microstructure with 4.7 % closed porosity (Fig. 7b) and 1.1 % small enclosed particles of a secondary phase with bright contrast, although no secondary phases were detected in the XRD analysis. The EDX measurement (Supplementary Figure 2) shows a higher concentration of lanthanum and oxygen in the secondary phase, with no changes in the distribution of the other elements, indicating residual La2O3 from the synthesis.

The sintered separators ball-milled with a high Li₂CO₃ content of 10

mol % (Li₂CO₃@BM) and a low Li₂CO₃ content of 5 mol % (Li₂CO₃@BM-L) were analyzed electrochemically. To determine the ionic conductivity, gold electrodes were sputtered onto the freshly sintered sample surface. In the Nyquist plots of the impedance spectra (Fig. 8a), only one semicircle is visible for both samples, which contains the contribution of both bulk and grain boundary resistance (capacitance of 3.57 10^{-10} F for BM-H and of 3.46 10^{-10} F for BM-L). The total ionic conductivity at room temperature derived from the low-frequency intercept is relatively similar for both tapes and is 0.16 mS cm⁻¹ for Li₂CO₃@BM-H and 0.18 mS cm⁻¹ for Li₂CO₃@BM-L tapes.

To test their suitability as battery separators, lithium plating and stripping tests were performed on the sintered tapes to determine the critical current density (CCD) for dendrite formation. The measurements were performed at 60 °C to increase the self-diffusion of lithium atoms while keeping the total amount of Lithium transferred in each cycle constant. To assemble a symmetrical Li||LLZO||Li cell, a 30 nm thin adhesive layer of gold was sputtered onto the tape surface to ensure good contact with the lithium electrodes. The Li foil was then mechanically attached to both sides of the separator and heated to melt the Lithium. Both the Li $_2\text{CO}_3$ @BM-H and Li $_2\text{CO}_3$ @BM-L samples were able to achieve the CCD value of 1 mA cm $^{-2}$ without dendrite formation, which is a very good performance for the thin tape-cast separators sintered without any pressure assistance (Fig. 8b, c). Interestingly, the separator prepared with less Li $_2\text{CO}_3$ in the ball milling step (Li $_2\text{CO}_3$ @BM-L) performs even better than the Li $_2\text{CO}_3$ @BM-L separator,

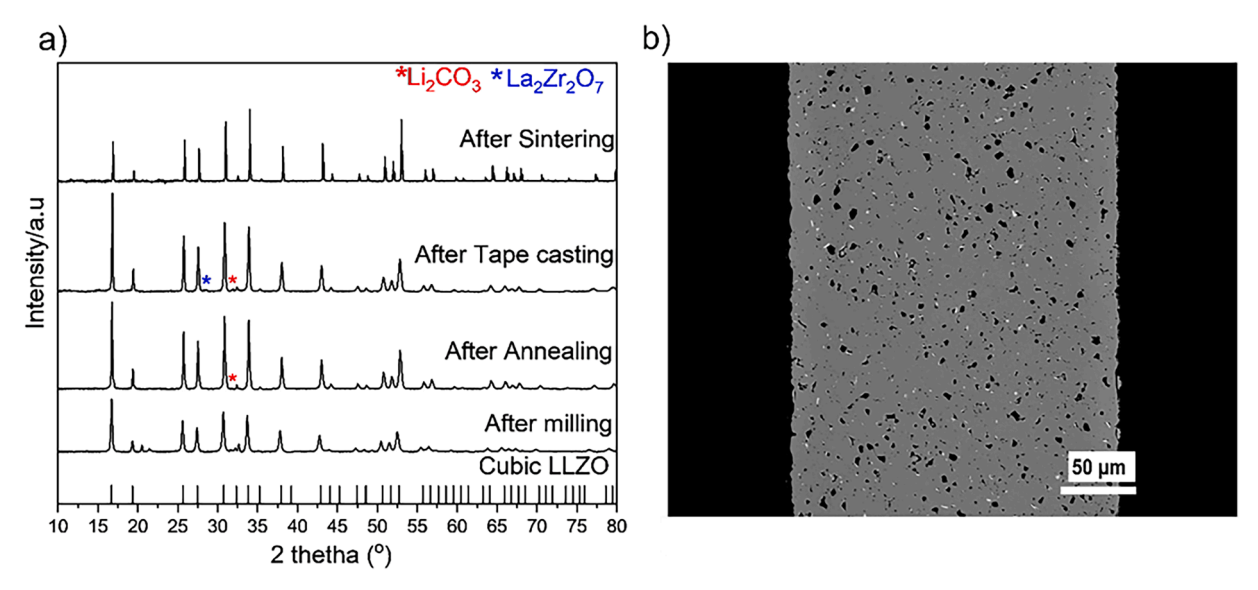


Fig. 7. a) XRD analysis of the primary process steps with lowered addition of Li₂CO₃; b) Cross-sectional SEM images of sintered BM-L separator.

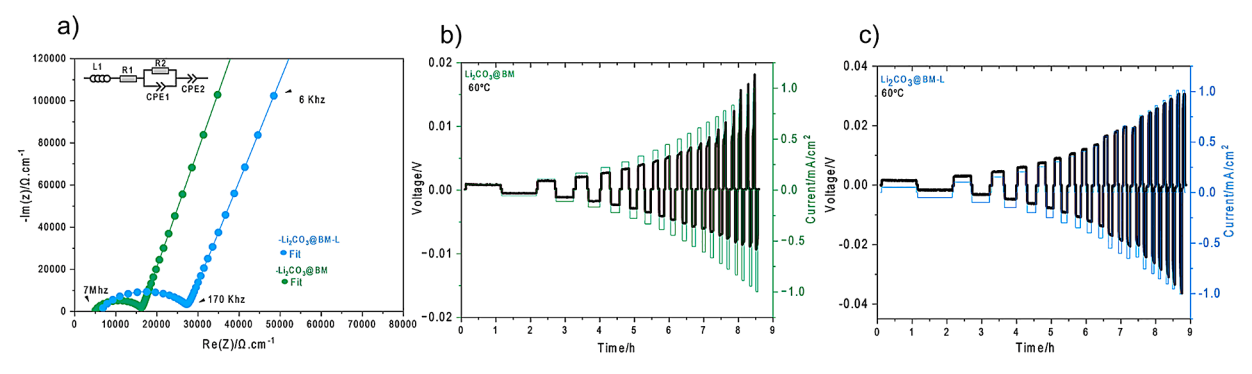


Fig. 8. a) Impedance spectra of the sintered Li₂CO₃@BM-H and Li₂CO₃@BM-L samples, normalized for sample thickness; b) CCD measurement of Li₂CO₃@BM-H; c) CCD measurement of Li₂CO₂@BM-I.

with flat potential steps and lower polarization despite its lower ionic conductivity.

Long-term cycling of the cells at current densities of 0.05 mA cm⁻², 0.1 mA cm⁻², 0.25 mA cm⁻², and 0.5 mA cm⁻² demonstrates stable cycling over 225 h with only minor polarization phenomena most likely connected to surface roughness and the electrode contacts (Fig. 9a,b).

The results of the electrochemical characterization show that the LLZO tapes produced with the optimized process described in this work are suitable for use as battery separators. It is expected that further optimization of the process would enable even smaller quantities of surplus lithium, which would further increase the economic attractiveness of this process.

4. Conclusions

In this work, we investigated the intricate relationship between the phase transformations of LLZO powder during the different steps of the tape-casting process and the morphology and properties of the resulting separators. By systematically investigating the influence of the degree of protonation during the different production steps, an effective approach was found to mitigate the degradation of the optimized LLZO powder with minimal excess Lithium. Our results show that the low mechanical stability and low ionic conductivity of ceramic separators after sintering are mainly due to the porous morphology caused by the protonation of LLZO during wet ball milling and insufficient compensation of Li loss during relithiation in the sintering step. Adding minimal amounts of Li₂CO₃ to the wet milling step shifted the balance of protonation,

ensuring the effectiveness of relithiation during subsequent thermal treatments. With a significantly reduced excess lithium of only 15 mol %, a dense, flat ceramic separator with an ionic conductivity of 0.13 mS cm $^{-1}$ was obtained, exhibiting a critical current density for Li dendrite formation of 1 mA cm $^{-2}$ at 60 $^{\circ}$ C.

CRediT authorship contribution statement

Kaouther Touidjine: Writing – review & editing, Writing – original draft, Visualization, Validation, Methodology, Investigation, Formal analysis, Conceptualization. Melanie Finsterbusch-Rosen: Writing – review & editing, Writing – original draft, Supervision, Investigation, Formal analysis. Vivien Kiyek: Writing – review & editing, Investigation, Formal analysis. Swapna Ganapathy: Writing – review & editing, Investigation, Formal analysis. Martin Finsterbusch: Writing – review & editing, Resources, Funding acquisition, Data curation. Olivier Guillon: Writing – review & editing, Supervision, Funding acquisition. Erik Kelder: Writing – review & editing, Supervision, Funding acquisition. Marnix Wagemaker: Writing – review & editing, Supervision, Funding acquisition. Dina Fattakhova-Rohlfing: Writing – review & editing, Writing – original draft, Supervision, Resources, Funding acquisition, Conceptualization.

Declaration of competing interest

The authors declare the following financial interests/personal relationships which may be considered as potential competing interests:

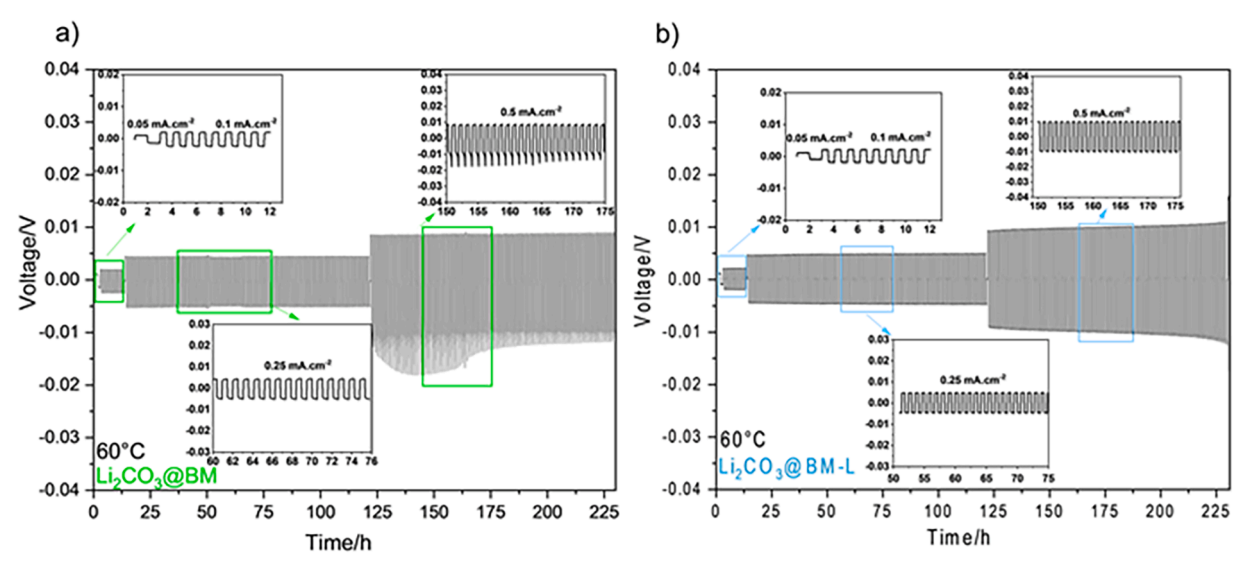


Fig. 9. Galvanostatic cycling of Li|LLZO|Li cells at 0.05 mA cm⁻², 0.1 mA cm⁻², 0.25 mA cm⁻², 0.5 mA cm⁻² at 60 °C: a) Li₂CO₃@BM, b) Li₂CO₃@BM-L.

Kaouther Touidjine reports financial support was provided by European Union's Horizon2020, DESTINY European doctorate program. Dina Fattakhova-Rohlfing reports financial support was provided by Federal Ministry of Education and Research Berlin Office. If there are other authors, they declare that they have no known competing financial interests or personal relationships that could have appeared to influence the work reported in this paper.

Acknowledgements

As a part of the DESTINY European doctorate program, the authors acknowledge funding from the European Union's Horizon2020 research and innovation program Under the Marie Skłodowska-Curie Actions COFUND-Grant Agreement No: 945357, and the Chairman Prof. Christian Masquelier. Financial support by the German Federal Ministry of Education and Research (BMBF) as part of the clusters of competencies Festbatt 2 (projects 13XP0434A and 13XP0432B) is gratefully acknowledged. The authors are indebted to Grit Häuschen for the LLZO powder synthesis and to Volker Bader for the sintering treatments operation; Mark Kwakernaak for contributing to the NMR discussion and Nahom Enkubahri for the help with the NMR software.

Supplementary materials

Supplementary material associated with this article can be found, in the online version, at doi:10.1016/j.ensm.2024.103487.

References

- M. Forsyth, L. Porcarelli, X. Wang, N. Goujon, D. Mecerreyes, Innovative electrolytes based on ionic liquids and polymers for next-generation solid-state batteries, Acc. Chem. Res. 52 (3) (2019) 686–694, https://doi.org/10.1021/acs. accounts 8b00566
- [2] J. Xiao, How lithium dendrites form in liquid batteries: studies of interfacial reactions and mass transport may allow safe use of lithium metal anodes, Science (1979) 366 (6464) (2019) 426–427, https://doi.org/10.1126/science.aay8672.
- [3] Y. Zhu, X. He, Y. Mo, Origin of outstanding stability in the lithium solid electrolyte materials: insights from thermodynamic analyses based on first-principles calculations, ACS. Appl. Mater. Interfaces. 7 (42) (2015) 23685–23693, https:// doi.org/10.1021/acsami.5b07517.
- [4] G.V Alexander, C. Shi, J. O'Neill, E.D Wachsman, Extreme lithium-metal cycling enabled by a mixed ion- and electron-conducting garnet three-dimensional architecture, Nat. Mater. 22 (9) (2023) 1136–1143, https://doi.org/10.1038/ s41563-023-01627-9.
- [5] M. Huang, T. Liu, Y. Deng, Effect of sintering temperature on structure and ionic conductivity of Li 7 XLa 3Zr 2O 12 0.5x ($x=0.5\sim0.7$) ceramics, Solid. State Ion. 204-205 (1) (2011) 41–45, https://doi.org/10.1016/j.ssi.2011.10.003.
- [6] S. Uhlenbruck, C. Dellen, S. Möller, Reactions of garnet-based solid-state lithium electrolytes with water — A depth-resolved study, Solid. State Ion. 320 (2018) 259–265, https://doi.org/10.1016/j.ssi.2018.03.004.
- [7] L. Cheng, E.J. Crumlin, W. Chen, The origin of high electrolyte-electrode interfacial resistances in lithium cells containing garnet type solid electrolytes, Phys. Chem. Chem. Phys. 16 (34) (2014) 18294–18300, https://doi.org/10.1039/c4cp02921f.
- [8] Y. Jin, P.J. McGinn, Li7La3Zr2O12 electrolyte stability in air and fabrication of a Li/Li7La3Zr 2O12/Cu0.1V2O5 solid-state battery, J. Power. Sources. 239 (2013) 326–331, https://doi.org/10.1016/j.jpowsour.2013.03.155.
- [9] W. Xia, B. Xu, H. Duan, Reaction mechanisms of lithium garnet pellets in ambient air: the effect of humidity and CO2, J. Am. Ceramic Society 100 (7) (2017) 2832–2839, https://doi.org/10.1111/jace.14865.
- [10] A. Sharafi, S. Yu, M. Naguib, Impact of air exposure and surface chemistry on Li-Li7La3Zr2O12 interfacial resistance, J. Mater. Chem. a Mater. 5 (26) (2017) 13475–13487. https://doi.org/10.1039/c7ta03162a.
- [11] W. Xia, B. Xu, H. Duan, Ionic conductivity and air stability of Al-Doped Li7La3Zr2O12 sintered in alumina and pt crucibles, ACS. Appl. Mater. Interfaces. 8 (8) (2016) 5335–5342, https://doi.org/10.1021/acsami.5b12186.
- [12] M. Nakayama, T. Horie, R. Natsume, Reaction kinetics of carbonation at the surface of garnet-type Li7La3Zr2O12 as solid electrolytes for all-solid-state li ion batteries, J. Phys. Chem. C 127 (16) (2023) 7595–7601, https://doi.org/10.1021/acs.
- [13] R. Grissa, S. Payandeh, M. Heinz, C. Battaglia, Impact of protonation on the electrochemical performance of Li7La3Zr2O12Garnets, ACS. Appl. Mater. Interfaces. 13 (12) (2021) 14700–14709, https://doi.org/10.1021/ acsami.0c23144.

- [14] Stephen Heywood, Matt Lessneier, David Driscoll, Stephen Sofie, Tailoring solid-state synthesis routes for high confidence production of phase pure, low impedance Al-LLZO Enhanced Reader, Am. Ceramic Soc. (2023), https://doi.org/10.1111/jace.18994. Published online.
- [15] E. Yi, W. Wang, J. Kieffer, R.M. Laine, Flame made nanoparticles permit processing of dense, flexible, Li+ conducting ceramic electrolyte thin films of cubic-Li7La3Zr2O12 (c-LLZO), J. Mater. Chem. a Mater. 4 (33) (2016) 12947–12954, https://doi.org/10.1039/c6ta04492a.
- [16] X. Xiang, F. Chen, Q. Shen, L. Zhang, C. Chen, Effect of the lithium ion concentration on the lithium ion conductivity of Ga-doped LLZO, Mater. Res. Express. 6 (8) (2019), https://doi.org/10.1088/2053-1591/ab2799.
- [17] N. Janani, S. Ramakumar, S. Kannan, R. Murugan, Optimization of lithium content and sintering aid for maximized Li+ conductivity and density in Ta-doped Li7La3Zr2O12, J. Am. Ceramic Soc. 98 (7) (2015) 2039–2046, https://doi.org/ 10.1111/jace.13578.
- [18] M. Mann, M. Küpers, G. Häuschen, M. Finsterbusch, D. Fattakhova-Rohlfing, O. Guillon, Evaluation of scalable synthesis methods for aluminum-substituted li7la3zr2o12 solid electrolytes, Materials (Basel) 14 (22) (2021), https://doi.org/ 10.3390/ma14226809.
- [19] K. Gao, M. He, Y. Li, Preparation of high-density garnet thin sheet electrolytes for all-solid-state Li-Metal batteries by tape-casting technique, J. Alloys. Compd. 791 (2019) 923–928, https://doi.org/10.1016/j.jallcom.2019.03.409.
- [20] Ruijie Ye, Water-based fabrication of garnet-based solid electrolyte separators for solid-state lithium batteries, Green chem. 22 (15) (2020) 4952–4961. Jg., Nr.S.
- [21] Melanie Rosen, Controlling the lithium proton exchange of LLZO to enable reproducible processing and performance optimization, J. Mater. Chem. A 9 (8) (2021) 4831–4840. Jg., NrS.
- [22] G.T. Hitz, High-rate lithium cycling in a scalable trilayer Li-garnet-electrolyte architecture, Mater. Today 22 (2019) 50–57.
- [23] L. Cheng, C.H. Wu, A. Jarry, Interrelationships among grain size, surface composition, air stability, and interfacial resistance of Al-substituted Li7La3Zr2O12 solid electrolytes, ACS. Appl. Mater. Interfaces. 7 (32) (2015) 17649–17655, https://doi.org/10.1021/acsami.5b02528.
- [24] C. Galven, J. Dittmer, E. Suard, F. Le Berre, M.P Crosnier-Lopez, Instability of lithium garnets against moisture. Structural characterization and dynamics of Li 7xH xLa 3Sn 2O 12 and Li 5-xH xLa 3Nb 2O 12, Chem. Mater. 24 (17) (2012) 3335–3345, https://doi.org/10.1021/cm300964k.
- [25] Understanding slurry formulations to guide sol_Re jui.
- [26] N.C. Rosero-Navarro, T. Yamashita, A. Miura, M. Higuchi, K. Tadanaga, Effect of sintering additives on relative density and li-ion conductivity of Nb-doped Li7La3ZrO12 solid electrolyte, J. Am. Ceramic Society 100 (1) (2017) 276–285, https://doi.org/10.1111/jace.14572.
- [27] Anthony Boulant, Jean Francois Bardeau, Alain Jouanneaux, Joel Emery, Jean-Yves Buzare, Odile Bohnke, Reaction mechanism of LiO.3LaO.57TiO3 powder with ambient air: h+/Li+ exchqne with water and Li2CO3 formation, Dalton. Trans. 39 (2010) 3968–3975. https://doi.org/10.1039/b924684c, 2010:39(16):1-8.
- [28] A. Paolella, W. Zhu, G. Bertoni, Discovering the influence of lithium loss on garnet Li7La3Zr2O12electrolyte phase stability, ACS. Appl. Energy Mater. 3 (4) (2020) 3415–3424, https://doi.org/10.1021/acsaem.9b02401.
- [29] R.A. Jonson, E. Yi, F. Shen, M.C. Tucker, Optimization of tape casting for fabrication of Li6.25Al0.25La3Zr2O12Sheets, Energy Fuels 35 (10) (2021) 8982–8990, https://doi.org/10.1021/acs.energyfuels.1c00566.
- [30] E. Hanc, W. Zajac, L. Lu, On fabrication procedures of Li-ion conducting garnets, J. Solid. State Chem. 248 (2017) 51–60, https://doi.org/10.1016/j. ices.2017.01.017
- [31] Y. Li, J.T. Han, C.A. Wang, H. Xie, J.B. Goodenough, Optimizing Li+ conductivity in a garnet framework, J. Mater. Chem. 22 (30) (2012) 15357–15361, https://doi. org/10.1039/c2im31413d.
- [32] G. Larraz, A. Orera, M.L. Sanjuán, Cubic phases of garnet-type Li7La3Zr 2012: the role of hydration, J. Mater. Chem. a Mater. 1 (37) (2013) 11419–11428, https://doi.org/10.1039/c3ta11996c.
- [33] L. Dhivya, R. Murugan, Effect of simultaneous substitution of y and Ta on the stabilization of cubic phase, microstructure, and Li+ conductivity of Li7La3Zr2O12 lithium garnet, ACS. Appl. Mater. Interfaces. 6 (20) (2014) 17606–17615, https:// doi.org/10.1021/am503731h.
- [34] C. Deviannapoorani, S. Ramakumar, N. Janani, R. Murugan, Synthesis of lithium garnets from La2Zr2O7 pyrochlore, Solid. State Ion. 283 (2015) 123–130, https:// doi.org/10.1016/j.ssi.2015.10.006.
- [35] L. Dhivya, K. Karthik, S. Ramakumar, R. Murugan, Facile synthesis of high lithium ion conductive cubic phase lithium garnets for electrochemical energy storage devices, RSC. Adv. 5 (116) (2015) 96042–96051, https://doi.org/10.1039/ c5ra18543h
- [36] L. Kong, I. Karatchevtseva, D.J. G.regg, M.G. Blackford, R. Holmes, G Triani, A novel chemical route to prepare La2Zr2O7 pyrochlore, J. Amer. Ceramic Soc. 96 (3) (2013) 935–941, https://doi.org/10.1111/jacc.12060.
- [37] G. Larraz, A. Orera, J. Sanz, I. Sobrados, V. Diez-Gómez, M.L. Sanjuán, NMR study of Li distribution in Li7-xHxLa3Zr2O12 garnets, J. Mater. Chem. a Mater. 3 (10) (2015) 5683–5691, https://doi.org/10.1039/c4ta04570j.
- [38] P. Ghorbanzade, A. Pesce, K. Gómez, Impact of thermal treatment on the Li-ion transport, interfacial properties, and composite preparation of LLZO garnets for solid-state electrolytes, J. Mater. Chem. a Mater. 11 (22) (2023) 11675–11683, https://doi.org/10.1039/d3ta01145c.